



**A Perturbation Solution to the Full Poisson-Nernst-Planck Equations Yields an Asymmetric Rectified Electric Field**

Journal:	<i>Soft Matter</i>
Manuscript ID	SM-ART-03-2020-000417.R2
Article Type:	Paper
Date Submitted by the Author:	02-May-2020
Complete List of Authors:	Hashemi Amrei, S. M. H.; University of California Davis College of Engineering, Chemical Engineering Miller, Gregory; University of California Davis College of Engineering, Chemical Engineering Bishop, Kyle; Columbia University, Chemical Engineering; Columbia University Ristenpart, William; University of California Davis College of Engineering, Chemical Engineering

# A Perturbation Solution to the Full Poisson-Nernst-Planck Equations Yields an Asymmetric Rectified Electric Field<sup>†</sup>

S. M. H. Hashemi Amrei,<sup>a</sup> Gregory H. Miller,<sup>a‡</sup> Kyle J. M. Bishop,<sup>b§</sup> and William D. Ristenpart<sup>a\*</sup>

We derive a perturbation solution to the one-dimensional Poisson-Nernst-Planck (PNP) equations between parallel electrodes under oscillatory polarization for arbitrary ionic mobilities and valences. Treating the applied potential as the perturbation parameter, we show that the second-order solution yields a nonzero time-average electric field at large distances from the electrodes, corroborating the recent discovery of Asymmetric Rectified Electric Fields (AREFs) via numerical solution to the full nonlinear PNP equations [Hashemi Amrei *et al. Phys. Rev. Lett.*, 2018, **121**, 185504]. Importantly, the first-order solution is analytic, while the second-order AREF is semi-analytic and obtained by numerically solving a single linear ordinary differential equation, obviating the need for full numerical solutions to the PNP equations. We demonstrate that at sufficiently high frequencies and electrode spacings the semi-analytical AREF accurately captures both the complicated shape and the magnitude of the AREF, even at large applied potentials.

## 1 Introduction

The dynamic response of a fluid to an applied oscillatory electric potential is of fundamental importance in many electrokinetic systems, including induced-charge electrokinetics (ICEK),<sup>1–5</sup> ac electroosmosis,<sup>6–9</sup> electrohydrodynamic manipulation of colloids,<sup>10–15</sup> electroconvection,<sup>16</sup> and ionic winds in atmospheric plasmas.<sup>17,18</sup> In continuum theory, analysis of such systems is based on the Poisson-Nernst-Planck (PNP) equations, also referred to as the standard electrokinetic model.<sup>19</sup> The Poisson equation relates the free charge density to the Laplacian of the electric potential via Gauss's law, and the transport of dissolved ions is governed by the electromigrative and diffusive fluxes.

The PNP equations are nonlinear and coupled; as a result, researchers have often invoked simplifying assumptions to solve them. The most common of these assumptions is that the applied potential ( $\phi_0$ ) is less than the thermal potential, i.e.,  $\phi_0 \ll k_B T/e$  where  $k_B$ ,  $T$ , and  $e$  are the Boltzmann constant, absolute temperature, and elementary charge, respectively. This assumption allows linearization of the problem via a perturbation expansion, written in terms of  $\Phi_0 = \phi_0 e / (k_B T) \ll 1$ . In most cases, the solution is assumed to include an equilibrium contribution (unperturbed) plus a perturbation linear in the applied potential (i.e., first-order expansion,  $O(\Phi_0)$ ). White and coworkers<sup>20–22</sup> and Hinch *et al.*<sup>23</sup> were among the first to follow this procedure in their analysis of dilute

colloidal suspensions, obtaining information about the dipole coefficient and electrophoretic mobility of spherical colloids subject to an oscillating electric field.

Researchers have also focused on finding the dynamic response of quiescent electrolytes (no colloids) between parallel electrodes. Hollingsworth and Saville<sup>24</sup> used a first-order perturbation expansion to derive an analytical approximate solution to the electric potential. Note that for a sinusoidal applied potential, a first-order perturbation expansion invariably yields a single-mode sinusoidal solution, albeit with a phase lag and amplitude that depend on location and system properties. It was later shown, however, that the nonlinear terms in the PNP equations yield multimodal solutions for  $\Phi_0 > 1$ .<sup>25–27</sup> Olesen *et al.*<sup>25</sup> numerically solved the PNP equations to show the significance of nonlinear terms at high potentials. This multimodal behavior, which was later corroborated by analytical solutions at asymptotically high<sup>26</sup> and moderate potentials,<sup>27</sup> casts doubt on the common interpretation of electrokinetic systems based on linearized theories.

Even more counterintuitively, recent work has revealed that electrolytes with non-equal mobilities generate multimodal electric fields with a long-range, nonzero time-average.<sup>28,29</sup> In other words, an oscillatory electric potential can induce a steady electric field within the liquid. Referred to as an Asymmetric Rectified Electric Field (AREF), the steady field in essence results from the mismatch in the ionic mobilities; the uneven magnitudes of the oscillatory motion of the ions give rise to a net free charge density, in turn creating a steady field component. The spatial distribution and magnitude of the AREF depends sensitively on the applied frequency and magnitude of the ionic mobility mismatch. Notably, the induced AREF persists several microns away from the electrodes, with a characteristic diffusive length scale  $\ell_D \sim 1–10 \mu\text{m}$ . This long-range behavior of AREF is at odds with the common assumption that most of the important electrokinetic phenomena

<sup>a</sup> Department of Chemical Engineering, University of California Davis, Davis, California 95616, United States.

<sup>b</sup> Department of Chemical Engineering, Columbia University, New York, New York 10027, United States.

<sup>‡</sup> grgmiller@ucdavis.edu

<sup>§</sup> kyle.bishop@columbia.edu

\* wristenpart@ucdavis.edu

<sup>†</sup> Electronic Supplementary Information (ESI) available: animated movie of the ions spatial distributions vs time. See DOI: 00.0000/00000000.

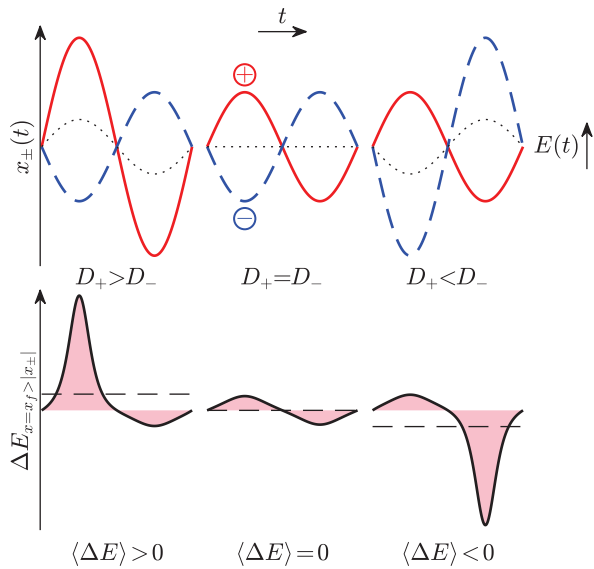


**Fig. 1** Two-ion model illustrating AREF. Top row: oscillation of a pair of ions ( $x_{\pm}$  vs time) with diffusivities  $D_{\pm}$  in response to an electric field  $E(t) = E_0 \cos(\omega t)$  for  $D_+ > D_-$ ,  $D_+ = D_-$ , and  $D_+ < D_-$ . The dotted curves show the oscillation of the center of charge. Bottom row: induced electric field ( $\Delta E$ ) at an arbitrary point  $x_f > |x_{\pm}|$  due to the ion oscillations vs. time. The horizontal dashed lines show the time-average electric field  $\langle \Delta E \rangle$ .

are governed solely by the Debye length scale ( $\kappa^{-1} \sim 1\text{--}100$  nm). Importantly, the calculated AREF is consistent with observations of colloidal levitation against gravity,<sup>30</sup> and is potentially responsible for the otherwise unexplained observations of flow reversal in ICEK systems.<sup>31</sup>

Hashemi Amrei et al. demonstrated that even a toy model of two ions undergoing asymmetric harmonic oscillation could yield an AREF.<sup>28</sup> Consider two ions, one positive and one negative, oscillating (as  $x_{\pm}(t)$ ) in response to an external sinusoidal electric field as illustrated in Fig. 1. When the two ions have equal diffusivities ( $D_+ = D_-$ ), they oscillate with the same amplitude in response to the external electric field. However, when there is a mismatch between the ion diffusivities, the fast moving ion undergoes an oscillation with a higher amplitude compared to the slow moving one. Then one can use Coulomb's law to evaluate an induced electric field ( $\Delta E$ ) due to the ion oscillations at an arbitrary point  $x_f > |x_{\pm}|$ . It turns out that when  $D_+ = D_-$ , the induced electric field is symmetrical in time with a zero time-average. However, for  $D_+ \neq D_-$ , a non-zero time-average electric field is induced. One can illustrate that this non-zero steady field component varies to leading order as the square of the applied field, i.e.,  $\Delta E \propto E_0^2$  (cf. Hashemi Amrei et al.<sup>28</sup>).

The two-ion model serves as a toy model only to provide some intuition about the importance of ionic mobility mismatch. As such, it lacks some fundamental aspects of an electrokinetic system such as the ion-ion interactions and the influence of thermal energy. To capture these effects, one must invoke the PNP equations. Consequently, all quantitative predictions to date have depended on complicated and time-consuming numerical solutions to the PNP equations. Progress assessing the impact of AREFs on

other systems has been hindered by the lack of analytical insight. Note that AREF is necessarily a nonlinear effect; therefore, first-order perturbation schemes cannot capture AREF, even when considering the asymmetry of electrolytes.<sup>20–23</sup> Additionally, Hashemi Amrei et al. demonstrated that AREF is identically zero for symmetric electrolytes,<sup>28,29</sup> as a result, prior studies considering the nonlinear effects at high potentials but neglecting the asymmetry of ions could not predict the AREFs either.<sup>25–27</sup> In short, only solutions to the full nonlinear PNP equations for asymmetric electrolytes predict AREF.

In this work, we provide a new, simpler, solution to the PNP equations for a 1-D system with arbitrary ionic mobilities and valences. We use a perturbation approach for small applied oscillatory potentials to find an exact analytical solution accurate to first-order. The first-order solution provides insight on how mobility mismatches alter the charge and potential distributions versus time and position. Furthermore, we derive a governing ordinary differential equation (ODE) for the time-average second-order solution, i.e., the AREF. We demonstrate that in the limit of small applied potentials this analytical AREF asymptotically converges in both spatial dependence and magnitude to numerical solutions of the full PNP equations. This approach yields the first independent theoretical corroboration of the existence of AREFs, and furthermore provides researchers with a rapid means of calculating the AREF without requiring a numerical solution to the full PNP system of equations.

The paper is organized as follows. We start by reviewing the PNP equations in Sec. 2. A detailed derivation of the approximate perturbation solution is provided in Sec. 3. The results for the first and second order solutions are presented and discussed in Sec. 4. We finish with some concluding remarks on the key results and implications for the electrokinetics community in Sec. 5.

## 2 Theory

### 2.1 Poisson-Nernst-Planck equations

We consider a binary electrolyte confined by two parallel electrodes separated by distance  $2\ell$  as depicted in Fig. 2. The Laplacian of the electric potential  $\phi(x, t)$  is related to the free charge density  $\rho(x, t)$  by the Poisson equation

$$-\epsilon \frac{\partial^2 \phi}{\partial x^2} = \rho = e(z_+ n_+ + z_- n_-). \quad (1)$$

Here subscripts  $\pm$  stand for positive and negative ions and the symbols denote liquid permittivity,  $\epsilon$ ; elementary charge,  $e$ ; charge numbers,  $z_{\pm}$ ; and ion concentrations,  $n_{\pm}$ . The transport of ions is governed by the Nernst-Planck equation

$$\frac{\partial n_{\pm}}{\partial t} + \frac{\partial j_{\pm}}{\partial x} = 0, \quad (2)$$

where the ion flux  $j_{\pm}(x, t)$  accounts for transport due both to diffusion and electromigration in the electric field:

$$j_{\pm}(x, t) = -D_{\pm} \frac{\partial n_{\pm}}{\partial x} - \frac{z_{\pm} e D_{\pm}}{k_B T} n_{\pm} \frac{\partial \phi}{\partial x}, \quad (3)$$

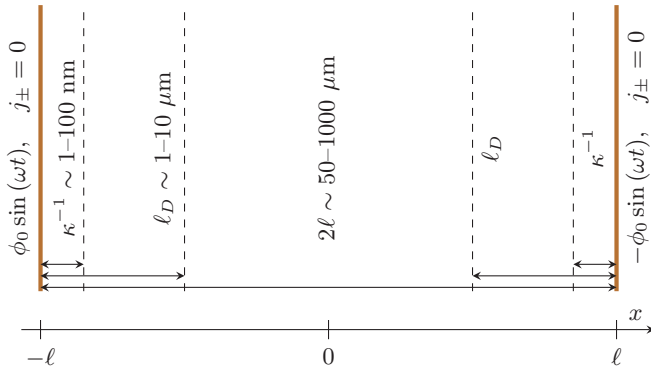


**Fig. 2** Schematic diagram of the problem and not-to-scale comparison of different characteristic length scales, i.e., Debye length ( $\kappa^{-1}$ ), diffusive length scale ( $\ell_D$ ), and electrode spacing ( $\ell$ ). A single-mode oscillatory electric potential of  $\mp\phi_0 \sin(\omega t)$  is applied on the parallel electrodes at  $x = \pm\ell$ .

where  $D_{\pm}$  and  $k_B T$  are the ion diffusivities and thermal energy, respectively.

Initially, no electric potential is applied and the electrolyte is spatially homogeneous,

$$n_{\pm}(x, 0) = n_{\pm}^{\infty} = \mp z_{\mp} n^{\infty}, \quad (4)$$

where  $n_{\infty}$  is the bulk number concentration of the electrolyte. An oscillatory potential of amplitude  $\phi_0$  and angular frequency  $\omega$  is applied across the electrodes such that

$$\phi(\pm\ell, t) = \mp\phi_0 \sin(\omega t). \quad (5)$$

Note that field-induced ion motion depends only on the potential gradient (not the potential itself). We can therefore measure the potential from any time-dependent reference we choose without altering the system dynamics. For example, we can add  $\phi_0 \sin(\omega t)$  to the applied potential at  $\pm\ell$  in eqn (5) to describe the common experimental scenario of a grounded electrode at one boundary (namely,  $x = \ell$ ). However, this antisymmetric boundary condition, along with placing the origin at the midplane and electrodes at  $x = \pm\ell$  (cf. Fig. 2), significantly simplifies the analytical analysis.

To close the problem, we assume no ion flux at the electrodes (i.e., no electrochemistry),

$$j_{\pm}(\pm\ell, t) = 0. \quad (6)$$

We acknowledge the fact that the assumption of negligible electrochemistry is justified only at low applied potentials. Additionally, we neglect the possible creation of a compact Stern layer at the electrodes which is known to cause a considerable potential drop between the electrode and electrolyte.<sup>25</sup> Also note that we focus on dilute electrolytes where the system dynamics is governed solely by the transport of the dissolved ions. For concentrated solutions, Stefan-Maxwell equations are required to account for the transport of all components including the solvent.<sup>32,33</sup>

## 2.2 Dimensionless form

The diffusivities  $D_+$  and  $D_-$  can be expressed by two parameters characterizing the diffusivity magnitude  $D$  and the diffusivity dif-

ference  $\beta$  as

$$D = \frac{2D_+ D_-}{D_+ + D_-} \quad \text{and} \quad \beta = \frac{D_+ - D_-}{D_+ + D_-}, \quad (7)$$

where  $-1 \leq \beta \leq 1$ . Similarly, the charge numbers  $z_+$  and  $z_-$  can be expressed by a magnitude parameter  $z$  and a difference parameter  $\gamma$ :

$$z = \frac{1}{2}(z_+ - z_-) \quad \text{and} \quad \gamma = \frac{z_+ + z_-}{z_+ - z_-}, \quad (8)$$

where  $-1 \leq \gamma \leq 1$ . Note that the charge numbers  $z_{\pm}$  are signed quantities and  $\gamma = 0$  for equal-valence ( $z_+ = -z_- = z$ ) electrolytes. The two difference parameters  $\beta$  and  $\gamma$  will play a central role in characterizing asymmetries in the binary electrolyte.

We nondimensionalize the governing equations using the following characteristic scales. Lengths are scaled by the Debye length

$$\kappa^{-1} = \sqrt{\frac{\epsilon k_B T}{2e^2 z^2 n_0}}, \quad (9)$$

where the concentration  $n_0$  is defined as

$$n_0 = \frac{1}{2z^2}(z_+^2 n_+^{\infty} + z_-^2 n_-^{\infty}) = \frac{1}{2z^2}(z_+ z_-^2 - z_+^2 z_-) n^{\infty}. \quad (10)$$

All concentrations are scaled by  $n_0$ . The electric potential is scaled by  $\phi_0 z e / (k_B T)$ , and time is scaled by  $1/(\kappa^2 D)$ . Using these scalings, the dimensionless variables are obtained as

$$\bar{x} = \kappa x, \quad \bar{t} = t \kappa^2 D, \quad \bar{n}_{\pm} = \frac{n_{\pm}}{n_0}, \quad \bar{\phi} = \frac{\phi z e}{k_B T}. \quad (11)$$

There are also five dimensionless parameters  $\beta$ ,  $\gamma$ ,  $\kappa\ell$ ,  $\Phi_0 = \phi_0 z e / (k_B T)$ , and  $\Omega = \omega / (\kappa^2 D)$  that uniquely describe the system.

Using the above dimensionless groups, the dimensionless governing equations become

$$\frac{\partial \bar{n}_{\pm}}{\partial \bar{t}} = \frac{1}{1 \mp \beta} \left[ \frac{\partial^2 \bar{n}_{\pm}}{\partial \bar{x}^2} \pm (1 \pm \gamma) \frac{\partial}{\partial \bar{x}} \left( \bar{n}_{\pm} \frac{\partial \bar{\phi}}{\partial \bar{x}} \right) \right], \quad (12)$$

$$-\frac{\partial^2 \bar{\phi}}{\partial \bar{x}^2} = \bar{\rho} = \frac{1}{2}(1 + \gamma)\bar{n}_+ - \frac{1}{2}(1 - \gamma)\bar{n}_-. \quad (13)$$

The dimensionless initial and boundary conditions are

$$\bar{n}_{\pm}(\bar{x}, 0) = \frac{1}{1 \pm \gamma}, \quad (14)$$

$$\bar{\phi}(\pm\kappa\ell, \bar{t}) = \mp\Phi_0 \sin(\Omega\bar{t}), \quad (15)$$

$$\bar{j}_{\pm}(\pm\kappa\ell, \bar{t}) = 0. \quad (16)$$

Here the dimensionless ion flux is

$$\bar{j}_{\pm} = \frac{j_{\pm}}{\kappa D n_0} = -\frac{1}{1 \mp \beta} \left[ \frac{\partial \bar{n}_{\pm}}{\partial \bar{x}} \pm (1 \pm \gamma) \left( \bar{n}_{\pm} \frac{\partial \bar{\phi}}{\partial \bar{x}} \right) \right]. \quad (17)$$

## 3 Approximate Solution

As discussed before, the system of equations given by eqns (12)–(16) is coupled and nonlinear with significant disparity of length and time scales. In particular, accounting for ionic mobility and valence mismatches complicates the numerical solution to the prob-

lem.<sup>28,29</sup> Alternatively, using a perturbation expansion, we can derive an approximate analytical solution that captures the system behavior, especially for asymmetric cases (i.e.,  $\beta \neq 0$  and/or  $\gamma \neq 0$ ).

### 3.1 Perturbation expansion in $\Phi_0$

In the limit of small potentials ( $\Phi_0 \ll 1$ ), the solution can be approximated by the power series

$$\tilde{n}_\pm(\tilde{x}, \tilde{t}) = \tilde{n}_\pm^{(0)}(\tilde{x}, \tilde{t}) + \Phi_0 \tilde{n}_\pm^{(1)}(\tilde{x}, \tilde{t}) + \Phi_0^2 \tilde{n}_\pm^{(2)}(\tilde{x}, \tilde{t}) + \dots \quad (18)$$

$$\tilde{\phi}(\tilde{x}, \tilde{t}) = \tilde{\phi}^{(0)}(\tilde{x}, \tilde{t}) + \Phi_0 \tilde{\phi}^{(1)}(\tilde{x}, \tilde{t}) + \Phi_0^2 \tilde{\phi}^{(2)}(\tilde{x}, \tilde{t}) + \dots \quad (19)$$

We substitute these expansions into the governing equations and initial/boundary conditions, and collect like powers of  $\Phi_0$ . Below, we solve for the zeroth-order solution, the first-order solution, and the time-average second-order electric field.

#### 3.1.1 Zeroth-order

One can show that the zeroth-order solution is simply

$$\tilde{n}_\pm^{(0)}(\tilde{x}, \tilde{t}) = \frac{1}{1 \mp \gamma}, \quad (20)$$

$$\tilde{\phi}^{(0)}(\tilde{x}, \tilde{t}) = 0. \quad (21)$$

Here, we have neglected the intrinsic zeta potential of the electrodes for simplicity. Therefore, the zeroth-order solution is specified by the initial conditions of the problem. However, inclusion of a zeta potential is straightforward; the zeroth-order solution can be replaced by an analytical solution to the equilibrium problem with constant potential boundary condition. Nonetheless, we should emphasize that this assumption affects only the solution at the Debye scale (close to the electrodes), while we are particularly interested in the behavior of the system at the micron scale (several Debye lengths to microns away from the electrodes).

#### 3.1.2 First-order

Using the zeroth-order solution, the first-order system of equations can be expressed as

$$\frac{\partial \tilde{n}_\pm^{(1)}}{\partial \tilde{t}} + \frac{\partial \tilde{j}_\pm^{(1)}}{\partial \tilde{x}} = 0, \quad (22)$$

$$-\frac{\partial^2 \tilde{\phi}^{(1)}}{\partial \tilde{x}^2} = \frac{1}{2}(1 + \gamma)\tilde{n}_+^{(1)} - \frac{1}{2}(1 - \gamma)\tilde{n}_-^{(1)}, \quad (23)$$

subject to the following boundary conditions:

$$\tilde{\phi}^{(1)}(\pm \kappa \ell, \tilde{t}) = \mp \sin(\Omega \tilde{t}), \quad (24a)$$

$$\tilde{j}_\pm^{(1)}(\pm \kappa \ell, \tilde{t}) = 0. \quad (24b)$$

Here, the first-order ion flux  $\tilde{j}_\pm^{(1)}(\tilde{x}, \tilde{t})$  is

$$\tilde{j}_\pm^{(1)}(\tilde{x}, \tilde{t}) = -\frac{1}{1 \mp \beta} \left[ \frac{\partial \tilde{n}_\pm^{(1)}}{\partial \tilde{x}} \pm \frac{\partial \tilde{\phi}^{(1)}}{\partial \tilde{x}} \right]. \quad (25)$$

We consider solutions of the form

$$\tilde{n}_\pm^{(1)}(\tilde{x}, \tilde{t}) = \text{Im} \left[ \hat{n}_\pm^{(1)}(\tilde{x}) e^{i\Omega \tilde{t}} \right], \quad \tilde{\phi}^{(1)}(\tilde{x}, \tilde{t}) = \text{Im} \left[ \hat{\phi}^{(1)}(\tilde{x}) e^{i\Omega \tilde{t}} \right]. \quad (26)$$

The complex amplitudes  $\hat{n}_\pm^{(1)}(\tilde{x})$  and  $\hat{\phi}^{(1)}(\tilde{x})$  are governed by

$$i\Omega \hat{n}_\pm^{(1)} = \frac{1}{1 \mp \beta} \left[ \frac{\partial^2 \hat{n}_\pm^{(1)}}{\partial \tilde{x}^2} \pm \frac{\partial^2 \hat{\phi}^{(1)}}{\partial \tilde{x}^2} \right], \quad (27)$$

$$-\frac{\partial^2 \hat{\phi}^{(1)}}{\partial \tilde{x}^2} = \frac{1}{2}(1 + \gamma)\hat{n}_+^{(1)} - \frac{1}{2}(1 - \gamma)\hat{n}_-^{(1)}. \quad (28)$$

The corresponding boundary conditions are

$$\hat{\phi}^{(1)}(\pm \kappa \ell) = \mp 1, \quad (29a)$$

$$-\frac{1}{1 \mp \beta} \left[ \frac{\partial \hat{n}_\pm^{(1)}}{\partial \tilde{x}} \pm \frac{\partial \hat{\phi}^{(1)}}{\partial \tilde{x}} \right]_{\pm \kappa \ell} = 0. \quad (29b)$$

Note that this problem has odd symmetry about  $\tilde{x} = 0$  ( $\hat{n}_\pm^{(1)}(0) = \hat{\phi}^{(1)}(0) = 0$ ). Substituting eqn (28) for the potential into eqn (27) for the ion concentrations, we obtain an eigenvalue problem from which one can derive the following solution for  $\hat{n}_\pm^{(1)}(\tilde{x})$

$$\hat{n}_+^{(1)}(\tilde{x}) = A(-\gamma + s) \sinh(\lambda_- \tilde{x}) + B(1 - \gamma) \sinh(\lambda_+ \tilde{x}), \quad (30)$$

$$\hat{n}_-^{(1)}(\tilde{x}) = A(1 + \gamma) \sinh(\lambda_- \tilde{x}) - B(-\gamma + s) \sinh(\lambda_+ \tilde{x}), \quad (31)$$

with

$$s = 2i\beta\Omega + \sqrt{\Delta}, \quad (32a)$$

$$\Delta = 1 - 4\beta\Omega(i\gamma + \beta\Omega). \quad (32b)$$

The eigenvalues  $\lambda_\pm$  are

$$\lambda_\pm = \frac{1}{\sqrt{2}} \left( 1 + 2i\Omega \pm \sqrt{\Delta} \right)^{1/2}. \quad (33)$$

Substituting the solutions from eqns (30) and (31) for the ion concentrations into eqn (28) and subsequent integration yields

$$\begin{aligned} \hat{\phi}^{(1)}(\tilde{x}) = & Cx - A(1 + \gamma)(s - 1) \frac{\sinh(\lambda_- \tilde{x})}{2\lambda_-^2} \\ & - B(1 - \gamma)(s + 1) \frac{\sinh(\lambda_+ \tilde{x})}{2\lambda_+^2}. \end{aligned} \quad (34)$$

The constants A, B, and C are determined by the boundary conditions at  $\tilde{x} = \kappa \ell$ :

$$A = \frac{s - 1}{\lambda_- \kappa \ell \cosh(\lambda_- \kappa \ell) \Gamma}, \quad B = \frac{s + 1}{\lambda_+ \kappa \ell \cosh(\lambda_+ \kappa \ell) \Gamma}, \quad (35)$$

$$\begin{aligned} C = \frac{1}{\kappa \ell} \left( -1 + A(1 + \gamma)(s - 1) \frac{\sinh(\lambda_- \kappa \ell)}{2\lambda_-^2} \right. \\ \left. + B(1 - \gamma)(s + 1) \frac{\sinh(\lambda_+ \kappa \ell)}{2\lambda_+^2} \right). \end{aligned} \quad (36)$$

Here the parameter  $\Gamma$  is

$$\begin{aligned} \Gamma = s^2 - 2\gamma s + 1 - \frac{1}{2\kappa \ell} \left[ \frac{(\gamma + 1)(s - 1)^2 (\lambda_- \kappa \ell - \tanh(\lambda_- \kappa \ell))}{\lambda_-^3} \right. \\ \left. - \frac{(\gamma - 1)(s + 1)^2 (\lambda_+ \kappa \ell - \tanh(\lambda_+ \kappa \ell))}{\lambda_+^3} \right]. \end{aligned} \quad (37)$$

Finally, having the zeroth and first order perturbation terms, the overall first-order solution (denoted by superscript [1]) becomes:

$$\tilde{n}_{\pm}^{[1]}(\bar{x}, \bar{t}) = \tilde{n}_{\pm}^{(0)}(\bar{x}, \bar{t}) + \Phi_0 \tilde{n}_{\pm}^{(1)}(\bar{x}, \bar{t}), \quad (38)$$

$$\tilde{\phi}^{[1]}(\bar{x}, \bar{t}) = \tilde{\phi}^{(0)}(\bar{x}, \bar{t}) + \Phi_0 \tilde{\phi}^{(1)}(\bar{x}, \bar{t}). \quad (39)$$

One can show that for the special case of symmetric electrolytes (i.e.,  $\beta = \gamma = 0$ ), this first-order solution becomes identical to the solution provided by Hollinsworth and Saville.<sup>24</sup>

Note that many electrolytes have  $z_+ = |z_-|$  for which  $\gamma = 0$  (e.g., NaCl, NaOH, KCl, KOH, etc.). For such electrolytes,  $\Delta = 1 - 4\beta^2\Omega^2$  (cf. eqn (32b)). Then an interesting case occurs when  $\beta^2\Omega^2 = \frac{1}{4}$ , yielding  $\Delta = 0$  and hence,  $\lambda_+ = \lambda_-$ . In this case a separate solution is necessary; please see Appendix B for details. Our independent numerical calculations (not shown) and our separate analytical solution (Appendix B) indicate that the solution behavior does not qualitatively change when  $\gamma = 0$  and  $\beta^2\Omega^2 = \frac{1}{4}$ , i.e., there is no special physical significance to this combination of parameter values.

### 3.1.3 Second-order

The second-order governing equations for  $\tilde{n}_{\pm}^{(2)}$  and  $\tilde{\phi}^{(2)}$  are

$$\frac{\partial \tilde{n}_{\pm}^{(2)}}{\partial \bar{t}} + \frac{\partial \tilde{j}_{\pm}^{(2)}}{\partial \bar{x}} = 0, \quad (40)$$

$$-\frac{\partial^2 \tilde{\phi}^{(2)}}{\partial \bar{x}^2} = \frac{1}{2}(1 + \gamma)\tilde{n}_+^{(2)} - \frac{1}{2}(1 - \gamma)\tilde{n}_-^{(2)}, \quad (41)$$

where

$$\tilde{j}_{\pm}^{(2)}(\bar{x}, \bar{t}) = -\frac{1}{1 \mp \beta} \left[ \frac{\partial \tilde{n}_{\pm}^{(2)}}{\partial \bar{x}} \pm \frac{\partial \tilde{\phi}^{(2)}}{\partial \bar{x}} \pm (1 \pm \gamma)\tilde{n}_{\pm}^{(1)} \frac{\partial \tilde{\phi}^{(1)}}{\partial \bar{x}} \right]. \quad (42)$$

The boundary conditions are

$$\tilde{\phi}^{(2)}(\pm \kappa \ell, \bar{t}) = 0, \quad (43a)$$

$$\tilde{j}_{\pm}^{(2)}(\pm \kappa \ell, \bar{t}) = 0. \quad (43b)$$

One can show that the time-average of eqn (40) over a period of the applied potential (i.e.,  $\bar{t} = 0$  to  $2\pi/\Omega$ ) yields:

$$\frac{\partial \langle \tilde{j}_{\pm}^{(2)} \rangle}{\partial \bar{x}} = 0, \rightarrow \langle \tilde{j}_{\pm}^{(2)} \rangle = \text{constant} \quad (44)$$

with

$$\langle \tilde{j}_{\pm}^{(2)} \rangle = -\frac{1}{1 \mp \beta} \left[ \frac{\partial \langle \tilde{n}_{\pm}^{(2)} \rangle}{\partial \bar{x}} \pm \frac{\partial \langle \tilde{\phi}^{(2)} \rangle}{\partial \bar{x}} \mp \frac{1}{4}(1 \pm \gamma) \left( \hat{n}_{\pm}^{(1)} \bar{E}^{(1)} + \bar{n}_{\pm}^{(1)} \hat{E}^{(1)} \right) \right]. \quad (45)$$

Here  $\langle X \rangle$  is the time-average of  $X$ ,  $\hat{E}^{(1)} = -\partial \hat{\phi}^{(1)}/\partial \bar{x}$ , and overbars denote complex conjugates, e.g.,  $\bar{E}^{(1)} = \text{conj}(\hat{E}^{(1)})$ . All electric fields ( $E = -\partial \phi/\partial x$ ) are scaled by  $k_B T \kappa/(ze)$ .

Note that eqn (44) combined with the time-average of the ion

flux boundary condition (i.e.,  $\langle \tilde{j}_{\pm}^{(2)} \rangle_{\pm \kappa \ell} = 0$ ) imply that  $\langle \tilde{j}_{\pm}^{(2)} \rangle = 0$  everywhere. Therefore using eqn (45) one can write

$$\frac{\partial \langle \tilde{n}_{\pm}^{(2)} \rangle}{\partial \bar{x}} = \pm \langle \bar{E}^{(2)} \rangle \pm \frac{1}{4}(1 \pm \gamma) \left( \hat{n}_{\pm}^{(1)} \bar{E}^{(1)} + \bar{n}_{\pm}^{(1)} \hat{E}^{(1)} \right). \quad (46)$$

On the other hand, the time-average of eqn (41) becomes

$$-\frac{\partial^2 \langle \tilde{\phi}^{(2)} \rangle}{\partial \bar{x}^2} = \frac{1}{2}(1 + \gamma)\langle \tilde{n}_+^{(2)} \rangle - \frac{1}{2}(1 - \gamma)\langle \tilde{n}_-^{(2)} \rangle, \quad (47)$$

which can be differentiated with respect to  $\bar{x}$  as

$$\frac{\partial^2 \langle \bar{E}^{(2)} \rangle}{\partial \bar{x}^2} = \frac{1}{2}(1 + \gamma) \frac{\partial \langle \tilde{n}_+^{(2)} \rangle}{\partial \bar{x}} - \frac{1}{2}(1 - \gamma) \frac{\partial \langle \tilde{n}_-^{(2)} \rangle}{\partial \bar{x}}. \quad (48)$$

Then substituting  $\partial \langle \tilde{n}_{\pm}^{(2)} \rangle / \partial \bar{x}$  from eqn (46) yields the following ODE for the time-average electric field:

$$\frac{\partial^2 \langle \bar{E}^{(2)} \rangle}{\partial \bar{x}^2} - \langle \bar{E}^{(2)} \rangle = f, \quad (49)$$

where

$$f = \frac{1}{8} \left[ \left( (1 + \gamma)^2 \hat{n}_+^{(1)} + (1 - \gamma)^2 \hat{n}_-^{(1)} \right) \bar{E}^{(1)} + \left( (1 + \gamma)^2 \bar{n}_+^{(1)} + (1 - \gamma)^2 \bar{n}_-^{(1)} \right) \hat{E}^{(1)} \right]. \quad (50)$$

At the boundaries  $\bar{x} = \pm \kappa \ell$ , we assume  $\langle \bar{E}^{(2)} \rangle_{\pm \kappa \ell} = 0$  to close the problem. Note that this assumption is consistent with all of our numerical solutions for single-mode sinusoidal applied potentials.

The right hand side  $f$  in eqn (49) is known from the first-order solution. However we could not find an explicit expression for this complicated function in terms of the dimensionless parameters and variables. Therefore, we numerically solve this ODE to find a semi-analytical approximation to AREF. (Please refer to Appendix A for details of the corresponding numerical solution.)

## 4 Results and Discussion

In the following subsections, we present and discuss the results of first-order and second-order solutions, focusing mainly on the impacts of  $\beta$  and  $\gamma$ . We also compare these low-potential approximate solutions with the numerical solution to the full nonlinear PNP equations. For visual purposes, we change the origin of the spatial domain from midplane to the left electrode, i.e.,  $y = x + \ell$  with  $y \in [0, 2\ell]$ .

### 4.1 First-order solution

Fig. 3 compares the first-order (eqns (38) and (39)) and numerical solutions to the ion concentrations and electric potential at different voltages. (Detail of the numerical solution algorithm are provided elsewhere.<sup>28</sup>) The values are normalized by  $\Phi_0$  to render the analytical solution independent of the applied potential. Time variations of excess positive and negative ion concentrations and electric potential are depicted in Fig. 3(a)–(c) at a certain location of  $\kappa y = 1$  (i.e., at the edge of the Debye layer). The highly multimodal numerical solutions approach the analytical solution by decreasing the applied potential to  $\Phi_0 \sim 1$ . As expected, the first-order analytical solution is sinusoidal, oscillating at the same

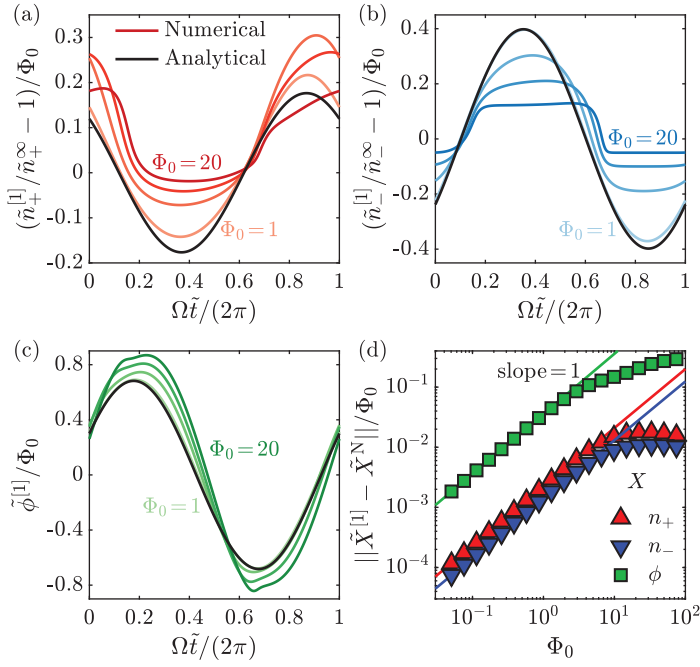


**Fig. 3** Comparison of the first-order approximate and full numerical solutions to the PNP equations. (a,b,c) Time variations of the normalized ion concentrations (a, b) and potential (c) for the approximate solution and numerical solution at different potentials ( $\Phi_0 = 20, 10, 5, 1$ ), evaluated at a fixed location of  $\kappa y = 1$  (i.e., one Debye layer away from the left electrode). (d) Normalized norm of the difference between approximate and numerical solutions vs potential. Parameters:  $\beta = -1/3$ ,  $\gamma = -1/3$ ,  $\kappa\ell = 100$ ,  $\Omega = 0.01$ .

frequency as the applied potential (i.e.,  $\Omega$ ), with its amplitude and phase lag depending on location and other dimensionless groups. Fig. 3(d) quantitatively compares the numerical and analytical solutions in the time and space domains. The integral norm of the difference, defined as

$$\|\tilde{X}^{[1]} - \tilde{X}^N\| = \frac{1}{(2\kappa\ell)(\frac{2\pi}{\Omega})} \int_0^{\frac{2\pi}{\Omega}} \int_0^{2\kappa\ell} |\tilde{X}^{[1]} - \tilde{X}^N|_{y,\tilde{t}} d\tilde{y}d\tilde{t}, \quad (51)$$

is plotted against  $\Phi_0$ , where the superscripts [1] and N denote the first-order and numerical solutions, respectively, and  $X = n_{\pm}, \phi$ . Note that the observed convergence rate is  $O(\Phi_0)$  as expected for this first-order approximation.

The effect of  $\beta$  on the first-order solution is demonstrated in Fig. 4 for  $\gamma = 0$ . The excess ion concentrations, free charge density, and electric potential are shown vs position at a certain time of  $\Omega\tilde{t} = \pi/2$  (i.e., when the applied potential reaches to its peak magnitude). For symmetric electrolytes ( $\beta = 0$ , thick black curves) the ion concentrations reach to the bulk values after a few Debye layers. However, for  $\beta \neq 0$ , where there is a mismatch between the mobilities of ions, a non-monotonic behavior is observed. The ion concentrations oscillate spatially with an amplitude decaying to zero at the midplane (Fig. 4(a) and (b)). (Please see the supplementary animated movie for the time variations of the spatial distributions.<sup>†</sup>) Far away from the electrode (insets in Fig. 4(a) and (b)), the negative and positive ions appear to have the same distribution and dependency on the  $\beta$  value. But an analysis of the

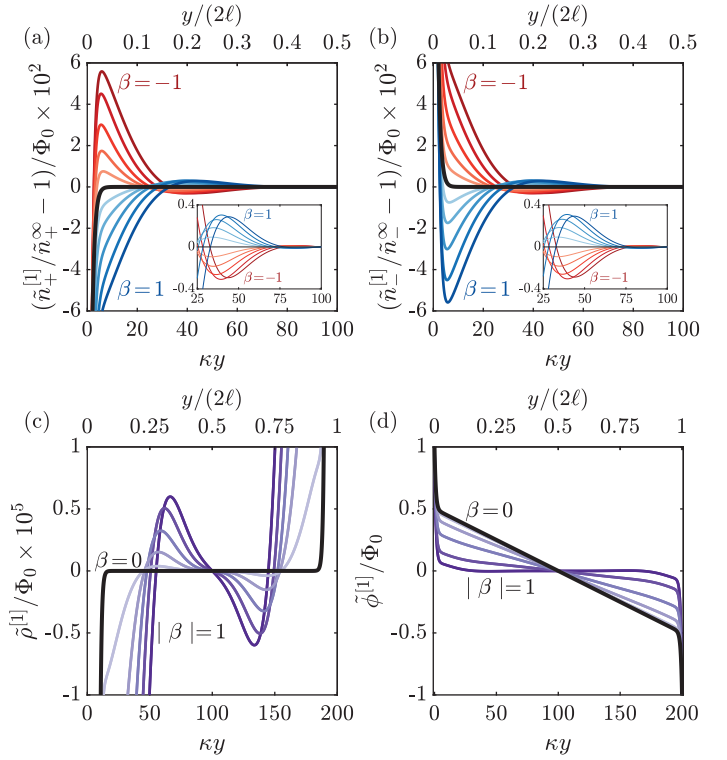


**Fig. 4** Effect of  $\beta$  on the first-order solution. Spatial variations of the normalized positive and negative ion concentrations (a,b), free charge density (c), and potential (d) for different  $\beta$ , evaluated at a fixed time of  $\Omega\tilde{t} = \pi/2$ . The black curves in all figures correspond to  $\beta = 0$ . Note that the insets in (a) and (b) look very similar but are quantitatively distinct. Parameters:  $\gamma = 0$ ,  $\kappa\ell = 100$ ,  $\Omega = 0.01$ .

free charge density distribution ( $\rho^{[1]}$ ) reveals a systematic difference (Fig. 4(c)). For a symmetric electrolyte the free charge density approaches to zero after a few Debye layers. For  $\beta \neq 0$  however,  $\rho^{[1]}$  spatially oscillates to become identically zero at the midplane. Note that the free charge density is three orders of magnitude smaller than the nominal ion concentrations. However it was shown that, despite its small magnitude, it yields electrophoretic forces (AREF-induced) that are several orders of magnitude higher than gravitational and colloidal forces in electrokinetic systems.<sup>28</sup> Finally, Fig. 4(d) shows the impact of  $\beta$  on the electric potential distribution. Regardless of  $\beta$ , a considerable portion of the potential drop occurs within a few Debye layers from the electrodes. The screening strength of the Debye layer seems to increase for  $\beta \neq 0$ , further dropping the potential toward zero in the bulk.

Fig. 5(a) shows the impact of  $\gamma$  on the free charge density distribution for  $\beta = 0$  and  $-1/2$ . We consider the most common values of  $\gamma = -1/3, 0, 1/3$  which correspond to 1-2, 1-1, and 2-1 electrolytes, respectively. Interestingly, when  $\beta = 0$ ,  $\gamma$  has no effect on the spatial distribution of free charge density. Similar to the results illustrated in Fig. 4(c),  $\rho^{[1]}$  approaches to zero within a few Debye layers away from the electrodes. When  $\beta \neq 0$ , the valence mismatch becomes important. For this representative example shown in Fig. 5(a),  $\gamma$  can even qualitatively change the spatial oscillation of the distribution, e.g., dashed red curve ( $\gamma = -1/3$ ) changes sign (charge reversal) near the midplane which does not happen for the

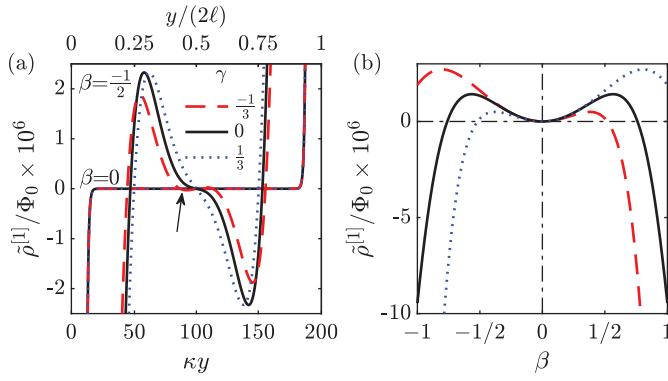


**Fig. 5** Effects of  $\gamma$  and  $\beta$  on the first-order solution. (a) Spatial variations of the normalized free charge density for different  $\gamma$  and two different  $\beta$  values of 0 and  $-1/2$ , evaluated at a fixed time of  $\Omega\bar{t} = \pi/2$ . The arrow points to the tiny charge reversal that occurs for  $\beta = -1/2, \gamma = -1/3$  near the midplane. (b) Normalized Free charge density vs  $\beta$  for different  $\gamma$  values, evaluated at fixed time and location of  $\Omega\bar{t} = \pi/2$  and  $\kappa y = 50$ . Parameters:  $\kappa\ell = 100, \Omega = 0.01$ .

other two  $\gamma$  cases. Note that depending on the applied frequency and the electrolyte type, multiple charge reversals can occur. The results presented here serve as a representative example. (Please see Hashemi Amrei et al.<sup>29</sup> for a detailed analysis of charge reversals.) Additionally,  $\gamma = 0$  seems to provide the maximum nonzero free charge density in the bulk. A notable observation in Fig. 4(c) and (d) is that  $|\beta|$  (not  $\beta$ ) governs the system behavior. For example, cases of  $\beta = -1/3$  ( $D_- = 2D_+$ ) and  $\beta = 1/3$  ( $D_+ = 2D_-$ ) yield the same results. As shown in Fig. 5(b), this behavior breaks when  $\gamma \neq 0$ . At fixed location of  $\kappa y = 50$  and time of  $\Omega\bar{t} = \pi/2$ , the free charge density is plotted vs  $\beta$  for different  $\gamma$  values. We notice that for  $\gamma = 0$ , it is the absolute value of  $\beta$  that determines the system behavior, consistent with the results in Fig. 4(c). But when  $\gamma \neq 0$ , the corresponding curves of positive and negative  $\gamma$  are mirrored about  $\beta = 0$ , and the system is governed by the product  $\beta\gamma$ . Moreover, for  $\beta = 0$ , the free charge density at the micron scale is zero for all  $\gamma$  values, in accordance to the spatial distributions in Fig. 5(a).

#### 4.2 Second-order solution

The semi-analytical AREF from eqn (49) is compared to that obtained from numerical solution to the PNP equations in Fig. 6 at different applied potentials. Hereafter, we refer to these two AREFs as semi-analytical ( $\langle \bar{E} \rangle^{\text{SA}}$ ) and numerical ( $\langle \bar{E} \rangle^{\text{N}}$ ), respectively. The AREF is normalized by  $\Phi_0^2$  to make the semi-analytical AREF independent of the applied potential. (Note that  $\langle \bar{E} \rangle^{\text{SA}} = \Phi_0^2 \langle \bar{E}^{(2)} \rangle$ .) Fig. 6(a) shows the comparison for  $\Omega = 0.001$ . We realize that as  $\Phi_0$  gets smaller, the numerical AREF approaches to the semi-analytical one. More importantly at the micron scale, which is of interest to most researchers, the semi-analytical solution accurately captures the complicated spatial structure of AREF. As a matter of fact, the curves of different  $\Phi_0$  collapse under appropriate normalization. This behavior is robust, even at higher frequencies (Fig. 6(b)) where AREF has multiple sign changes. In other words, the semi-analytical solution correctly predicts the AREF sign and

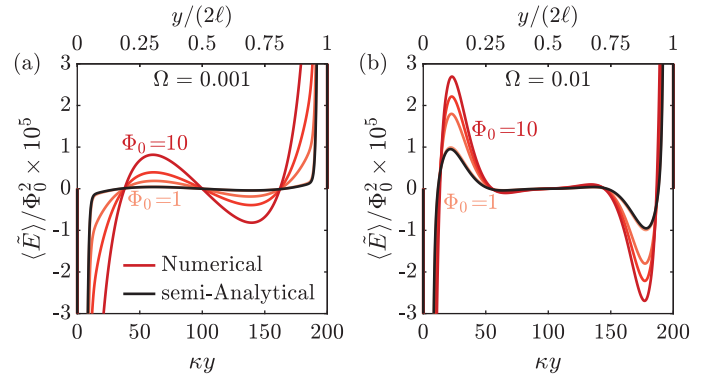


**Fig. 6** Comparison of the second-order approximate (semi-analytical) and numerically calculated AREF (i.e., time-average electric field,  $\langle \bar{E} \rangle$ ). Spatial variations of the normalized AREF for approximate solution and numerical solution at different potentials ( $\Phi_0 = 10, 7, 5, 1$ ) and for  $\Omega = 0.001$  (a) and  $\Omega = 0.01$  (b). Parameters:  $\beta = -1/3, \gamma = -1/3, \kappa\ell = 100$ .

zeros. Therefore, instead of the complicated numerical solution to the PNP equations, researchers can safely use this approximation to find the direction of AREF-induced electrophoretic force. (We will discuss these issues in more detail; cf. Fig. 9 and the corresponding discussion.)

We have analyzed the impact of  $\beta$  on the semi-analytical AREF in Fig. 7 when  $\gamma = 0$  and  $-1/3$ . For  $\gamma = 0$ , Fig. 7(a) and (b) show a non-monotonic  $\beta$  dependence of the AREF peak magnitude. By increasing the  $|\beta|$  from 0 (identically zero AREF) to 1, AREF peak magnitude at the micron scale first ascends to a maximum and then drops. Notably, when  $|\beta| \rightarrow 1$  the spatial structure is significantly affected and the peak disappears (curves *a* and *f* in Fig. 7(a) and (b), respectively). Similar observations were reported for the numerical AREF calculation.<sup>29</sup> The problem gets more intricate for a nonzero  $\gamma$ . A representative case of  $\gamma = -1/3$  is depicted in Fig. 7(c) and (d). When  $\beta < 0$ , changing the  $\gamma$  from 0 to  $-1/3$  slightly affects the AREF distribution, decreasing its magnitude (cf. curves in Fig. 7(a) and (c)). However, when  $\beta > 0$ , a qualitative difference is observed between cases of  $\gamma = 0$  and  $-1/3$  (e.g., compare *j* curves in Fig. 7(b) and (d)). As pointed out by Hashemi Amrei et al.,<sup>29</sup> when the faster ion has a smaller valence (and vice versa), there will be a competition between ionic mobility and valence mismatches to determine the sign of AREF. In the context of this study, the competition exists when  $\beta\gamma < 0$ . When  $\beta\gamma > 0$ , the both sources of asymmetry work in accord to determine the AREF sign. Another notable observation is that when  $\beta = 0$ , regardless of  $\gamma$ , AREF is identically zero at the micron scale.

It would be helpful to compare the AREF for actual electrolytes of different  $(\beta, \gamma)$  combinations (Fig. 8). The diffusivity of an ion can be expressed in terms of its drag coefficient ( $\lambda_i$ ) as<sup>20,23,24</sup>

$$D_i = \frac{k_B T}{\lambda_i}, \quad \lambda_i = \frac{N_A e^2 |z_i|}{\Lambda_i^\infty}, \quad (52)$$

where  $\Lambda_i^\infty$  is the limiting conductance of the ion and  $N_A$  is the Avogadro's number. Limiting conductance data of different ions can be found in physical chemistry textbooks.<sup>34</sup> NaOH has the highest negative  $\beta$  value ( $D_- > D_+$ ) among the selected electrolytes

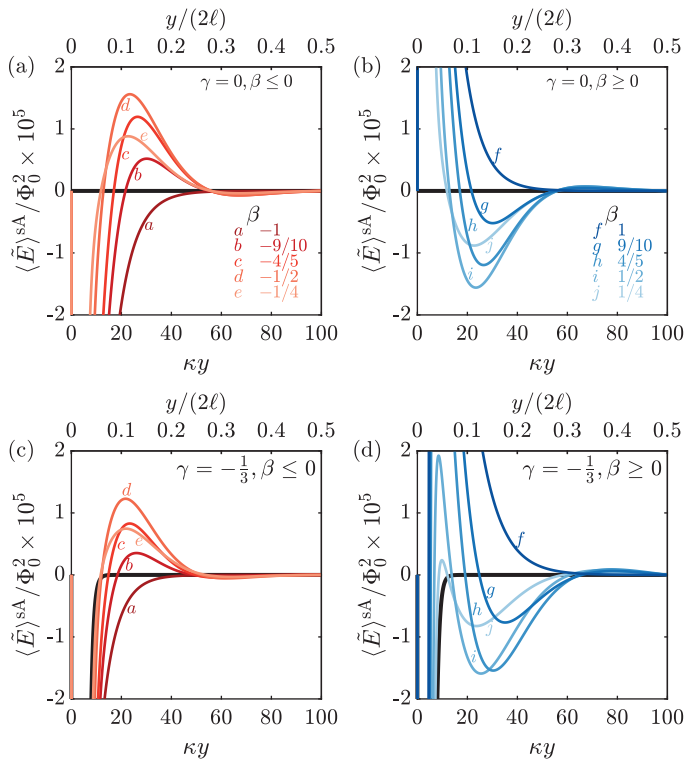


**Fig. 7** Effect of  $\beta$  on the second-order approximate (semi-analytical) AREF (i.e., time-average electric field,  $\langle \tilde{E} \rangle$ ) for  $\gamma = 0$  (a,b) and  $\gamma = -1/3$  (c,d). The black curves in all figures correspond to  $\beta = 0$ . Parameters:  $\kappa\ell = 100$ ,  $\Omega = 0.01$ .

and provides the maximum positive peak. As  $\beta$  gets closer to zero, the AREF peaks at lower magnitudes; e.g., compare NaCl with  $\beta = -0.21$  to NaOH with  $\beta = -0.6$ . As expected, electrolytes with positive  $\beta$  (HCl,  $\beta = 0.64$ ) have negative peaks. An interesting case would be KCl with a nearly zero ionic mobility mismatch ( $\beta = -0.02$ ) for which the AREF is nearly zero. However, recall that the  $\beta$  effect on AREF peak magnitude is non-monotonic (Fig. 7), a behavior that was explained at length by Hashemi Amrei et al.<sup>29</sup> Using a different set of dimensionless parameters (e.g.,  $\delta = D_-/D_+$  instead of  $\beta$  as a measure for ionic mobility mismatch), they showed that  $\delta_{\max}$  for which AREF has its maximum peak depends on  $\Phi_0$ . By increasing  $\Phi_0$ ,  $\delta_{\max}$  gets indefinitely closer to 1 (equivalently,  $\beta_{\max}$  gets closer to 0). Therefore, at high applied potentials, KCl may have a higher peak than NaOH. It is worth mentioning that for the dimensionless parameters used in the present study, the  $\beta_{\max}$  is not governed solely by  $\Phi_0$ . Finally, electrolytes with valence mismatch ( $\gamma \neq 0$ ) show intriguing behavior (CaCl<sub>2</sub> and H<sub>2</sub>SO<sub>4</sub>). As discussed in discussion of Fig. 7, a balance between asymmetries due to  $\beta$  and  $\gamma$  determines the AREF distribution.

Finally, we comprehensively analyze the collapse of numerical AREF curves for different potentials in Fig. 9. Fig. 9(a) shows the numerical AREF distribution for different voltages normalized by their corresponding peak values (dashed curves of different color intensities), along with the semi-analytical AREF plotted as solid. Each color corresponds to a different dimensionless frequency ( $\Omega$ ). We notice that by increasing the  $\Omega$ , a better collapse is obtained.

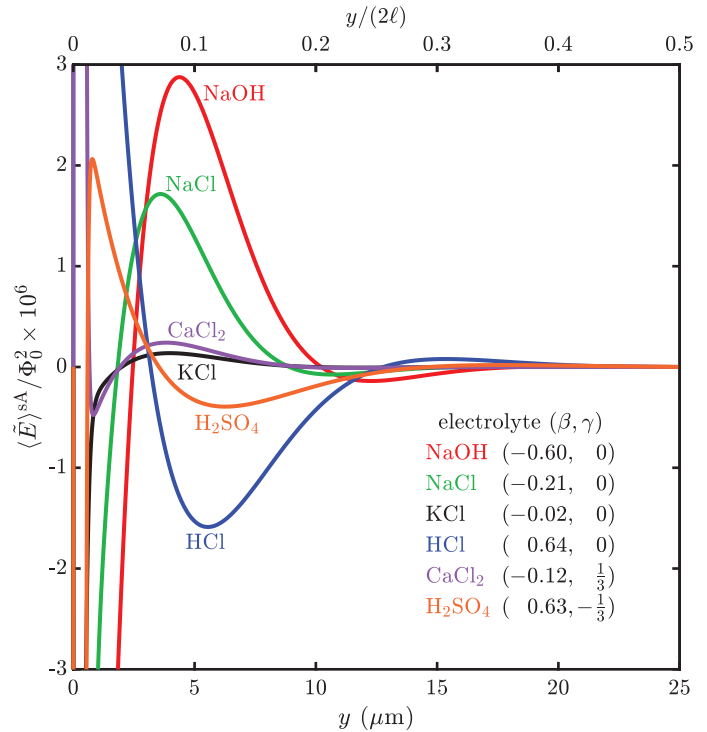


**Fig. 8** Spatial variations of the second-order approximate (semi-analytical) AREF (i.e., time-average electric field,  $\langle \tilde{E} \rangle$ ) for different electrolytes. Dimensional parameters:  $\ell = 25 \mu\text{m}$ ,  $\varepsilon = 78$ ,  $T = 298.15 \text{ K}$ ,  $n^\infty = 6.022 \times 10^{21} \text{ m}^{-3}$  ( $10^{-5} \text{ M}$ ),  $f = 100 \text{ kHz}$ .

Additionally, the ratio of numerical to semi-analytical AREF peak is plotted versus  $\Phi_0$  in Fig. 9(b) for different  $\Omega$ . Interestingly, as  $\Omega$  increases, the ratio decays to nearly 1, even at very high voltages. We perform a similar analysis by changing the  $\kappa\ell$ . We find that collapse of data improves by increasing the  $\kappa\ell$  value (Fig. 9(c)). Moreover, semi-analytical solution appears to accurately predict the AREF peak magnitude at high  $\kappa\ell$  (Fig. 9(d)). Therefore, we conclude that at high  $\Omega$  and  $\kappa\ell$  values, semi-analytical solution accurately captures 1) the spatial structure of AREF (better collapse), and 2) the AREF magnitude.

It appears that regardless of the system properties, there is a ‘threshold’  $\Phi_0$  above which the numerical AREF curves do not collapse, and this threshold tends to increase with  $\Omega$  or  $\kappa\ell$ . At low applied potentials and fixed other system properties, all AREF distributions collapse onto the semi-analytical solution; but as  $\Phi_0$  passes the threshold potential, the shape of AREF at the micron scale starts deviating from the semi-analytical solution. For sufficiently large  $\Omega$  or  $\kappa\ell$  values, this threshold potential is simply beyond the considered  $\Phi_0$  range. However, the underlying physics behind the collapse of the AREF distributions and its sensitivity to  $\Omega$  and  $\kappa\ell$  remain unclear.

Parameters  $\Omega$  and  $\kappa\ell$  can be combined into one dimensionless parameter as

$$\mathcal{L}_D = \frac{\ell_D}{\ell} = \sqrt{\frac{1}{\Omega(\kappa\ell)^2}} = \frac{\sqrt{D/\omega}}{\ell}. \quad (53)$$



case, the general solution to the first-order problem becomes:

$$\hat{n}_+^{(1)}(\bar{x}) = A \sinh(\lambda \bar{x}) - \frac{iS}{4\lambda} (A+B) \bar{x} \cosh(\lambda \bar{x}), \quad (\text{B1})$$

$$\hat{n}_-^{(1)}(\bar{x}) = iSB \sinh(\lambda \bar{x}) - \frac{1}{4\lambda} (A+B) \bar{x} \cosh(\lambda \bar{x}), \quad (\text{B2})$$

$$\hat{\phi}^{(1)}(\bar{x}) = Cx + (iSB - A) \frac{\sinh(\lambda \bar{x})}{2\lambda^2} + (A+B)(iS - 1) \frac{\lambda \bar{x} \cosh(\lambda \bar{x}) - 2 \sinh(\lambda \bar{x})}{8\lambda^4}. \quad (\text{B3})$$

with

$$\lambda = \frac{1}{\sqrt{2}} (1 + 2i\Omega)^{1/2}, \quad (\text{B4a})$$

$$S = \text{sgn}(\beta). \quad (\text{B4b})$$

The constants A, B, and C are determined as

$$A = \frac{4i\lambda^2}{\Gamma} \left[ \left( (4\lambda^2 - 1)S + i \right) \cosh(\lambda \kappa \ell) - (S - i)\lambda \kappa \ell \sinh(\lambda \kappa \ell) \right], \quad (\text{B5})$$

$$B = \frac{4i\lambda^2}{\Gamma} \left[ \left( S + (4\lambda^2 - 1)i \right) \cosh(\lambda \kappa \ell) + (S - i)\lambda \kappa \ell \sinh(\lambda \kappa \ell) \right], \quad (\text{B6})$$

$$C = -\frac{8iS\lambda (2\lambda^4 - 2\lambda^2 + 1) \cosh^2(\lambda \kappa \ell)}{\Gamma}. \quad (\text{B7})$$

The parameter  $\Gamma$  is

$$\Gamma = 2iS\lambda \kappa \ell \left[ 4(\lambda^4 - \lambda^2 + 1) + 2(2\lambda^4 - 2\lambda^2 + 1) \cosh(2\lambda \kappa \ell) + (4\lambda^2 - 3) \frac{\sinh(2\lambda \kappa \ell)}{\lambda \kappa \ell} \right]. \quad (\text{B8})$$

## References

- 1 N. I. Gamayunov, V. A. Murtsovkin and A. S. Dukhin, *Colloid J.*, 1986, **48**, 197–203.
- 2 A. S. Dukhin and V. A. Murtsovkin, *Colloid J.*, 1986, **48**, 203–209.
- 3 A. S. Dukhin, *Colloid J.*, 1986, **48**, 376–381.
- 4 M. Z. Bazant and T. M. Squires, *Phys. Rev. Lett.*, 2004, **92**, 066101.
- 5 T. M. Squires and M. Z. Bazant, *J. Fluid Mech.*, 2004, **509**, 217–252.
- 6 A. Ramos, H. Morgan, N. G. Green and A. Castellanos, *J. Phys. D: Appl. Phys.*, 1998, **31**, 2338–2353.
- 7 A. Ramos, H. Morgan, N. G. Green and A. Castellanos, *J. Colloid Interface Sci.*, 1999, **217**, 420–422.
- 8 A. Ajdari, *Phys. Rev. E*, 2000, **61**, R45(R).
- 9 V. Studer, A. Pepin, Y. Chen and A. Ajdari, *Analyst*, 2004, **129**, 944–949.
- 10 M. Trau, D. A. Saville and I. Aksay, *Science*, 1996, **272**, 706–709.
- 11 M. Trau, D. A. Saville and I. A. Aksay, *Langmuir*, 1997, **13**, 6375–6381.
- 12 D. C. Prieve, P. J. Sides and C. L. Wirth, *Curr. Opin. Colloid Interface Sci.*, 2010, **15**, 160–174.
- 13 F. Ma, S. Wang, L. Smith and N. Wu, *Adv. Funct. Mater.*, 2012, **22**, 4334–4343.
- 14 C. S. Dutcher, T. J. Woehl, N. H. Talken and W. D. Ristenpart, *Phys. Rev. Lett.*, 2013, **111**, 128302.
- 15 X. Yang and N. Wu, *Langmuir*, 2018, **34**, 952–960.
- 16 A. Mani and K. M. Wang, *Ann. Rev. Fluid Mech.*, 2020, **52**, 509–529.
- 17 A. M. Drews, L. Cademartiri, M. L. Chemama, M. P. Brenner, G. M. Whitesides and K. J. M. Bishop, *Phys. Rev. E*, 2012, **86**, 036314.
- 18 A. M. Drews, L. Cademartiri, G. M. Whitesides and K. J. M. Bishop, *J. Appl. Phys.*, 2013, **114**, 143302.
- 19 W. B. Russel, D. A. Saville and W. R. Schowalter, *Colloidal Dispersions*, Cambridge University Press, 1st edn, 1991.
- 20 E. H. B. Delacey and L. R. White, *J. Chem. Soc., Faraday Trans. 2*, 1981, **77**, 2007–2039.
- 21 C. S. Mangelsdorf and L. R. White, *J. Chem. Soc., Faraday Trans.*, 1992, **88**, 3567–3581.
- 22 C. S. Mangelsdorf and L. R. White, *J. Chem. Soc., Faraday Trans.*, 1997, **93**, 3145–3154.
- 23 E. J. Hinch, J. D. Sherwood, W. C. Chew and P. N. Sen, *J. Chem. SOC., Faraday Trans. 2*, 1984, **80**, 535–551.
- 24 A. D. Hollingsworth and D. A. Saville, *J. Colloid Interface Sci.*, 2003, **257**, 65–76.
- 25 L. H. Olesen, M. Z. Bazant and H. Bruus, *Phys. Rev. E*, 2010, **82**, 011501.
- 26 O. Schnitzer and E. Yariv, *Phys. Rev. E*, 2014, **89**, 032302.
- 27 R. F. Stout and A. S. Khair, *Phys. Rev. E*, 2015, **92**, 032305.
- 28 S. M. H. Hashemi Amrei, S. C. Bukosky, S. P. Rader, W. D. Ristenpart and G. H. Miller, *Phys. Rev. Lett.*, 2018, **121**, 185504.
- 29 S. M. H. Hashemi Amrei, G. H. Miller and W. D. Ristenpart, *Phys. Rev. E*, 2019, **99**, 062603.
- 30 S. C. Bukosky, S. M. H. Hashemi Amrei, S. P. Rader, J. Mora, G. H. Miller and W. D. Ristenpart, *Langmuir*, 2019, **35**, 6971–6980.

- 31 S. M. H. Hashemi Amrei, G. H. Miller and W. D. Ristenpart, *Phys. Rev. Fluids*, 2020, **5**, 013702.
- 32 S. T. P. Psaltis and T. W. Farrell, *J. Electrochem. Soc.*, 2011, **158**, A33–A42.
- 33 B. Balu and A. S. Khair, *Soft Matter*, 2018, **14**, 8267–8275.
- 34 A. W. Adamson, *A textbook of physical chemistry*, Academic Press, Inc., 2nd edn, 1979.

Induced steady field

Soft Matter

ac potential

Page 12 of 12

electrolyte

NaOH

NaCl

CaCl<sub>2</sub>

KCl

H<sub>2</sub>SO<sub>4</sub>

HCl

0

0

5

10

15

Distance from ac electrode ( $\mu\text{m}$ )

